embryos. The constant relationship between PL + CD and AB volumes implies that the PL volume is a dynamic variable, as required for a cytoplasmic lobe undergoing active protrusion and resorption.

As first cleavage is completed in modern lobe-forming embryos, the neck of the PL rapidly increases in diameter, leading to the formation of a J-shaped embryo until the CD cell finally absorbs the PL. About 39 J-shaped lobe-forming embryos can be identified on the basis of fossil shape. These are represented mainly by two different groups related to equal (Fig. 2, I to K) and unequal trefoil embryos (Fig. 2V), respectively. The smallest among the three parts of each embryo typically represents the PL. It can also be recognized by the presence of the PL constriction (PLC), which is relatively deeper than the cleavage furrow (CF) (Fig. 2I). The fully protruded lobe (Fig. 2K) is nearly equal in size to the CD cell.

During second cleavage of modern lobe-forming embryos, the last phase of lobe protrusion leads to the formation of a five-lobed morphology, which comprises the first four blastomeres of equal or subequal size and a PL protruding from the D cell. About 17 embryos are recognized to be fossil representatives of such five-lobed embryos (Fig. 2, W to Z). The lobes in these embryos are mostly uncompacted and nearly equal, with the smallest one corresponding possibly to the PL.

Lobe formation and retraction constitutes a symmetry-breaking device for the segregation of polar material to only one blastomere, an alternative to asymmetric cleavage. This mechanism is used today in disparate groups of mollusks including polyplacophorans, gastropods, scaphopods, and bivalves (14, 20–22), as well as a few types of annelids (*Chaetoplerus*) (14). The PL appears also in polyclad turbellarian flatworms (*Hoploplana inquilina*) (23, 24), which are widely accepted as a basal group of spiralians. In spiralian embryogenesis, the constituents of PL are required for specification of mesodermal structures and secondarily of other embryonic parts that are induced by mesoderm (15). That is, the blastomeres that receive the PL cytoplasm become mesoderm founder cells.

These fossil embryos may not be spiralians or spiralian ancestors, and indeed none of the later cleavage forms that have been recovered in the same deposits convincingly display the characteristic patterns of spiral cleavage (1, 8, 11). The most widespread and basal mode of embryogenesis in bilaterians operates by means of cleavage stage specification of blastomere fate, followed immediately by establishment of differential gene expression in the cell lineages descendant from these blastomeres (25, 26). The diverse territories of the embryo then soon express specific gene batteries generating a mosaic of differentiated cell types. This general mechanism is used in both direct and indirect

developing bilaterian forms. PL formation is only one of a great variety of mechanisms whose essential function is the asymmetric delivery of maternal components of regulatory importance to specific blastomeres (25, 26). In the case of the lobe-forming embryos studied here, the second cleavage lobe indicates that these embryos will specify one particular blastomere out of four that will be distinct in subsequent regulatory states. Only bilaterian embryos proceed in such a manner, but this is a typical bilaterian strategy of early development. Thus, these fossils imply that lobe formation is an ancient evolutionary device, and that the general strategy of precocious blastomere specification still used in most bilaterian groups was extant at least 40 million years before the Cambrian.

References and Notes

1. J.-Y. Chen, *The Dawn of Animal World* (Publishing House of Jiangsu Science & Technology, Nanjing, 2004).
2. X.-L. Yuan *et al.*, *Doushantuo Fossils: Life on the Eve of Animal Radiation* (Publishing House of Univ. of Science & Technology, Heifei, 2002).
3. D. Condon *et al.*, *Science* **308**, 95 (2005); published online 24 February 2005 (10.1126/science.1107765).
4. G. H. Barfod *et al.*, *Earth Planet. Sci. Lett.* **201**, 203 (2002).
5. C.-W. Li, J.-Y. Chen, T. Hua, *Science* **279**, 879 (1998).
6. J.-Y. Chen *et al.*, *Dev. Biol.* **248**, 182 (2002).
7. S. H. Xiao, X.-L. Yuan, A. H. Knoll, *Proc. Natl. Acad. Sci. U.S.A.* **97**, 13684 (2000).
8. J.-Y. Chen *et al.*, *Science* **305**, 218 (2004); published online 3 June 2004 (10.1126/science.1099213).
9. S. Bengtson, G. Budd, *Science* **306**, 1291a (2004).
10. J.-Y. Chen, P. Oliveri, E. Davidson, D. J. Bottjer, *Science* **306**, 1291b (2004).
11. J.-Y. Chen *et al.*, *Proc. Natl. Acad. Sci. U.S.A.* **97**, 4457 (2000).
12. S.-H. Xiao, Y. Zhang, A. H. Knoll, *Nature* **391**, 553 (1998).
13. S.-H. Xiao, A. H. Knoll, *J. Paleontol.* **74**, 767 (2000).
14. D. B. Conn, *Atlas of Invertebrate Reproduction and Development* (Wiley, Hoboken, NJ, ed. 2, 2000).
15. S. F. Gilbert, A. M. Raunio, Eds., *Embryology: Constructing the Organism* (Sinauer, Sunderland, MA, 1997).
16. G. W. Conrad *et al.*, *J. Cell Biol.* **59**, 228 (1979).
17. E. W. MacBride, *Text-Book of Embryology* (Macmillan, London, 1914).
18. L. W. Browder, C. A. Erickson, W. R. Jeffery, *Developmental Biology* (Saunders, Philadelphia, ed. 3, 1991).
19. See supplementary material on *Science* Online. The cleavage cells and the PLs in these embryos are either spherical or in compacted spherical form. The compacted form is regularly rounded in top view but has a relatively shorter radius in the distal-proximal direction. Cleavage cell and PL volumes were calculated as $4/3 \pi R^3$ in spherical forms (R, radius) and as $4/3 \pi R_1^2 R_2$ in compacted forms (R_1, noncompacted radius; R_2, compacted radius). The volumetric data of the embryos examined with SR-μCT (Fig. 2, B and I) were calculated precisely from the pixel number; each pixel bears a volume of 0.343 μm³.
20. A. C. Giese, J. S. Pearse, Eds., *Reproduction of Marine Invertebrates: Molluscs: Gastropods and Cephalopods* (Academic Press, New York, 1977).
21. A. C. Giese, J. S. Pearse, Eds., *Reproduction of Marine Invertebrates: Molluscs: Pelecypods and Lesser Classes* (Academic Press, New York, 1979).
22. A. S. Tompa, N. H. Verdonk, J. van den Biggelaar, Eds., *The Mollusca: Reproduction* (Academic Press, New York, 1984).
23. B. C. Boyer, *Int. J. Invertebr. Reprod. Dev.* **9**, 243 (1986).
24. B. C. Boyer, *Int. J. Invertebr. Reprod. Dev.* **13**, 157 (1988).
25. E. H. Davidson, *Gene Activity in Early Development* (Academic Press, Orlando, FL, 1986).
26. E. H. Davidson, *Genomic Regulatory Systems: Development and Evolution* (Academic Press, San Diego, CA, 2001).
27. Supported by Chinese Academy of Science grant KZCX3-SW-141; National Science Foundation of China grants 42432006, 40302004, 10490190, 60172042, and 10490194; 111 Project and 985-2 Project of Nanjing University, LPS of Nanjing Institute of Geology & Paleontology, NASA/Ames grant NAG2-1541, and an NSC grant. We thank the European Synchrotron Radiation Facility, Taiwan NSRRC, and Beijing Synchrotron Radiation Facility and Photon Factory for provision of synchrotron radiation facilities.

Element Partitioning: The Role of Melt Structure and Composition

M. W. Schmidt,[1]* J. A. D. Connolly,[1] D. Günther,[2] M. Bogaerts[1]

We segregated coexisting gabbroic and granitic melts by centrifuging them at high pressures and temperatures and measured the trace element compositions of the melts by laser ablation inductively coupled plasma mass spectrometry. Our results demonstrate that the effect of melt structure contributes about one order of magnitude to crystal/melt partition coefficients. Partitioning of alkali and alkaline earth elements strongly depends on field strength: Amphoteric and lone pair electron elements partition into the polymerized granitic melt; and rare earth, transition, and high field strength elements coordinated by nonbridging oxygens partition remarkably similar into the gabbroic melt. A regular solution model predicts these effects.

Element partitioning between magmas and crystals is essential to the differentiation of the Earth. Early work on trace element partitioning related mineral/melt partition coefficients, $D^{crystal/melt}$, to the relative ionic radii

of the trace and major elements (1, 2) and to melt composition (3, 4). The melt compositional term was simplified by normalizing to the partitioning of a major cation (3). By ascribing ideal mixing to the mineral component, which

expresses the behavior of the major cation in the melt, trace element partitioning can be formulated in terms of the lattice strain model (2, 5). This model defines a parabolic relationship between cation radius and partition coefficients that is specified by the effective Young's modulus, E, the partition coefficient, D_0, and the cation radius, r_0, relevant to the strain-free state. Although D_0 is dependent on melt composition, melt composition itself is not an explicit variable. Attempts to explicitly include melt composition in the lattice strain model were limited to specific compositional parameters such as H_2O content (6) and Fe/Mg ratio (7). Studies of coexisting silicate melts (8, 9) and mineral-melt systems suggest a strong dependence of crystal-melt partitioning on melt composition (10–15), but a general model for this dependence remains to be formulated.

In this study, we investigated partitioning of 45 elements between coexisting gabbroic and granitic K_2O-FeO-Al_2O_3-SiO_2 melts (16, 17) to isolate the effect of melt composition and structure from crystallographic effects. We used an experimental apparatus consisting of a piston cylinder mounted in a centrifuge that can achieve pressure and temperature conditions of 1.8 GPa and 1600°C, respectively, under an acceleration of 3000 g. Centrifuging is necessary to segregate coexisting silicate melts into pools large enough for measurement by laser ablation techniques, which permit simultaneous measurement of a large number of elements at trace-level concentrations [<200 parts per million (ppm)]. The centrifuging piston cylinder itself consists of a 42-kg integrated single-stage piston cylinder (18) with a 14-mm bore and 36-mm furnace length, allowing for capsules with an outer diameter of 4 mm and a length of 6 mm. The piston cylinder is mounted on a rotating 860-kg table with a 1.4-m diameter. With the sample at a radius of 32 cm, maximal acceleration of 3000 g is reached at 2850 revolutions per minute (rpm); at this frequency, the outer table rim travels at 753 km hour⁻¹.

Our experiments consisted of two steps: chemical equilibration (19) at the temperatures and pressures of interest (1100° to 1240°C and 0.3 to 0.7 GPa) at static conditions for 12 to 24 hours and physical segregation of the equilibrated melts by centrifuging for 3 to 14 hours at 600 to 1000 g. The experiments generated coexisting granitic and ferrogabbroic melts (Table 1). Additionally quartz, fayalite, or wuestite were sometimes present depending on composition and physical conditions. Centrifuging at 1000 g for >8 hours completely separated the melts (Fig. 1A) when crystals were absent; calculated

¹Institut für Mineralogie und Petrologie, Department of Earth Sciences, ²Department of Chemistry, Eidgenössische Technische Hochschule (ETH), 8092 Zürich, Switzerland.

*To whom correspondence should be addressed. E-mail: max.schmidt@erdw.ethz.ch

Table 1. Melt composition and polymerization of coexisting melts and comparison to natural melts. Z10 and Z18a represent the maximum and minimum width of the immiscibility gap at which segregation was achieved. Z10 pressure and temperature values were 0.7 GPa and 1180°C, respectively; for Z18a, they were 0.35 GPa and 1150°C. The difference in polymerization for the melt-pair of Z10 is similar to that of a primitive basaltic and a dacitic melt. The magnitude of D values measured in this study is thus representative of the span of melt compositions as to be expected in natural fractionation processes. NBO/T polymerization calculated after (27). x(NBO) is the molar fraction of nonbridging oxygens. x_{MO_n} is the molar fraction of major network-modifying component MO_n in our model. Picritic basalt is a representative for typical weakly polymerized mantle melt (33), whereas average granite is a representative for highly polymerized crustal melt (34). Dashed entry indicates oxide component is not present.

	Z10		Z18a		Natural picrobasalt	Natural alkaligranite
	Gabbroic	Granitic	Gabbroic	Granitic		
SiO_2	37.1	72.2	48.5	67.0	48.9	70.13
TiO_2	0.95	0.19	—	—	0.50	0.30
Al_2O_3	3.57	8.00	3.50	5.83	11.40	7.97
Fe_2O_3	—	—	—	—	1.3	2.77
FeO	51.4	11.5	45.0	21.1	8.8	5.27
MgO	—	—	—	—	14.7	0.07
CaO	—	—	—	—	10.3	0.55
Na_2O	—	—	—	—	1.84	7.46
K_2O	1.66	7.40	2.72	5.83	1.18	4.24
P_2O_5	1.77	0.21	0.10	0.03	0.25	0.26
Si*	2.236	3.320	2.719	3.234	2.392	3.239
$\Sigma(Fe^{3+} + Al)$*	0.254	0.433	0.231	0.332	0.705	0.495
$\Sigma(M^{2+})$*	2.594	0.442	2.107	0.852	1.979	0.278
$\Sigma(K+Na)$*	0.128	0.435	0.195	0.340	0.248	0.917
NBO/T	2.246	0.252	1.416	0.485	1.146	0.271
x(NBO)	0.699	0.118	0.522	0.216	0.443	0.127
x_{MO_n}	0.745	0.307	0.723	0.479	0.721	0.233
$x_{(NBO)}^{gabbro}/x_{(NBO)}^{granite}$	4.23		2.137		4.80	

*Atoms per eight oxygens.

density (20) differences between coexisting melts ranged from 0.45 to 0.95 g cm⁻³. In experiments at 600 to 800 g, a segregated gabbroic melt layer formed (Fig. 1B) with occasional quench fayalite or homogeneously distributed quench microdroplets (≤0.5 μm). In these experiments, the granitic melt, which is free of quench phases, contained quartz and gabbroic blobs, but blob- and quartz-free areas were large enough (up to 100 μm diameter) for laser ablation techniques. Large-diameter microprobe (10 μm) and laser ablation inductively coupled plasma mass spectrometry (LA-ICP-MS) analyses [20 to 40 μm spot size (18)] yielded homogeneous major and trace element compositions for the segregated gabbro and granite. In contrast, droplets that had not been segregated were heterogeneous (Fig. 1C) and composed of zones of internal droplets, fayalite needles with typical quench textures, and in some samples wuestite or Cr spinel. The internal droplets were <1 μm in size and may represent equilibrium inclusions of granitic melt or melt that exsolved during quenching.

The temperature range for segregation is limited by the critical temperature of the solvus at ~1200°C (21) and by abundant crystallization of fayalite and quartz at ≤1130°C. Although melt compositions that may be investigated are restricted to those on the miscibility gap, our melts are good proxies for gabbroic- and dacitic-to-granitic melts (Table 1). The network modifier Fe^{2+} in our synthetic system is an analog for the network modifiers Mg^+ Ca^+ Fe^{2+} in natural melts. Our experimental design ensures that all Fe is present as ferrous iron (18), thereby eliminating uncertainties that might arise from the presence of ferric iron, a network former. Trace elements are assumed to be present predominantly in their reduced form (i.e., Mn^{2+}, V^{3+} and V^{4+}, $Cr^{2+} > Cr^{3+}$, $Mo^{4+} > Mo^{5+}$, Sn^{2+}, Pb^{2+}, Ga^{3+}, As^{3+}, and Sb^{3+}).

The measured partition coefficients span two orders of magnitude (Fig. 2). Most amphoteric elements and heavy alkalis partition into the polymerized melt, with the lowest partition coefficient, $D^{gabbro/granite}$, values near 10^{-1} (Cs, As, and Pb). Most other metal cations concentrate in the depolymerized gabbroic melt, with the highest $D^{gabbro/granite}$ above 10 [rare earth elements (REE), U, and P]. On the basis of partitioning behavior, three groups of elements can be distinguished: (i) Alkalis and earth alkalis (except Mg), which have the lowest Pauling electronegativities (22) and field strengths (23, 24) of all elements investigated and form dominantly ionic bonds. This group shows a strong increase in $D^{gabbro/granite}$ with an increase

in electronegativity, field strength, or ionization potential ($D_{Cs} < D_{Rb} < D_K < D_{Na} < D_{Li} < D_{Ba} < D_{Sr} < D_{Ca}$), with Cs through Na partitioning into the polymerized melt. (ii) Amphoteric and lone electron pair elements (Ga, Ge, Sn^{2+}, Pb^{2+}, As^{3+}, Sb^{3+}, and Bi^{3+}) with electronegativities of 1.8 to 2.2. This group, which also includes Si and Al, substitutes into network-forming tetrahedra or has oxygen coordination numbers ≤ 4 (table S1) and partitions into the polymerized melt. (iii) RE, transition, and high field strength elements partitioning into the depolymerized melt with surprisingly uniform $D^{gabbro/granite}$ values (Fig. 2). Members of this group (Mg, Mn, Co, REE, Y, Sc, Ti, Th, U, Zr, Hf, V, Mo, and P) have coordination numbers ≥ 5 (table S1) except for Mo^{5+} and P^{5+}, which are predominantly fourfold coordinated but have two shells of nonbridging oxygens (NBOs) (25, 26), explaining their strong partitioning into the depolymerized melt. Among NBO-coordinated elements, rare earths exhibit the highest affinity for the depolymerized melt, and Zn, Zr, and Hf exhibit the lowest. REE have the highest (six- or sevenfold), and the mildly amphoteric element Zn the lowest, oxygen coordination numbers (fourfold), suggesting that coordination number influences partitioning behavior. Although the partitioning for the NBO-coordinated elements is similar, differences in geochemically similar elements such as Nb-Ta and Zr-Hf are systematic (Figs. 2 and 3B), elements with higher electronegativities exhibiting a preference for the depolymerized melt. The differences in Nb-Ta and Zr-Hf partitioning can cause relative enrichments, by fractionation, within these pairs by a factor of up to 1.6, an effect that would be substantial in geochemical modeling (11, 13, 14).

The partitioning behavior of the three element groups is explained by the different oxygen bonding environments in silicate melts (27). Bridging oxygens (BOs) shared by two network forming tetrahedra constitute the network of tetrahedrally coordinated cation sites occupied by Si and Al. Both Si and Al concentrate in the granitic melt, and elements coordinated by tetrahedral oxygens are conse-

quently also concentrated into the granitic melt. Among these, Ga^{3+} has the highest $D^{gabbro/granite}$, reflecting its relatively large ionic radius and its presence in both four- and sixfold coordination. Oxygens belonging to tetrahedra occupied by Al are charge-deficient and obtain charge compensation through alkalis and, to a lesser extent, by earth alkalis. Our data demonstrate that the elements with the highest degree of ionic bonding are preferred for this charge-compensating role. The affinity within the alkali and earth alkali groups for the depolymerized melt increases regularly with decreasing atomic number and radius. For these two groups, the effect of melt composition influences both the position and shape of the lattice strain parabola. The largest divalent cations, Ba and Pb, have, for different reasons, the lowest $D^{gabbro/granite}$ with respect to other divalent cations. Because of their extreme size, these elements exert a strong influence on the definition of the divalent cation lattice strain parabola. Apart from the alkalis and alkalis earth, coordination with charge-deficient tetrahedral oxygens may also influence the behavior of amphoteric elements Pb^{2+}, Sn^{2+}, As^{3+}, and Sb^{3+}, contributing to their preference for the polymerized melt. Lastly, the third group of elements, with oxygen coordination numbers ≥ 4 and that partition into the depolymerized melt, is controlled by the abundance of nonbridging oxygens, which permit cations to form their preferred coordination polyhedra. Field strength does not play an important role for the elements partitioning into NBO-coordinated sites, in contrast to interpretations from early melt-melt partitioning studies (8, 9) but in agreement with the data on the limited number of elements that were measured in both earlier data sets.

Values of the partition coefficients depend on the solvus width. Previous descriptions of melt-melt element partitioning used a two-
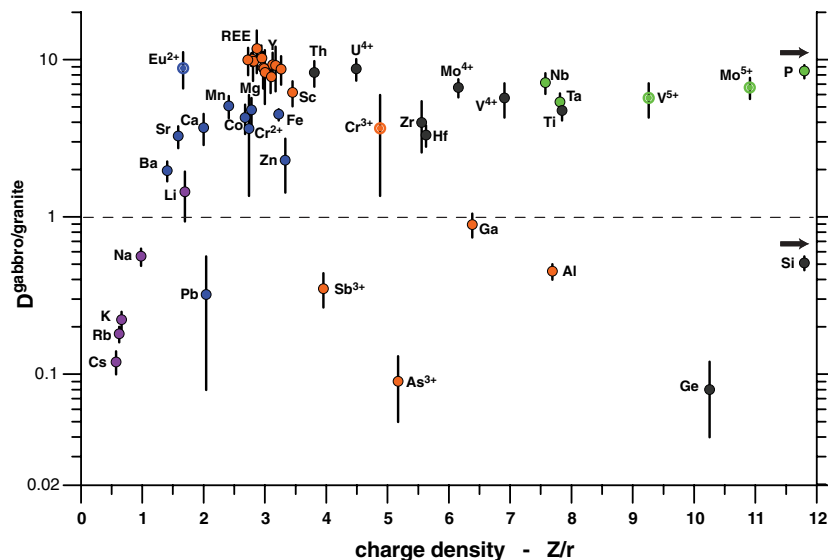
Fig. 2. Nernst partition coefficients, $D^{gabbro/granite}$, between gabbroic and granitic melt versus field strength (Z/r) for the experiment at 1180°C and 0.7 GPa (Z10). P ($Z/r = 34.6$) and Si ($Z/r = 15.4$) are off the scale. Cations that may have two major oxidation states are given with both values; the predominant oxidation state has a solid symbol.

Fig. 1. Textures of segregated and nonsegregated coexisting silicate melts. (**A**) Full segregation at 1150°C, 0.3 GPa, 12 hours static, and 9 hours at 1000 g (Z18a) for Mo in Pt double capsule. The bright left side is Fe-rich gabbroic, the dark side granitic melt. (**B**) Partial segregation at 1180°C, 0.7 GPa, 12 hours static, and 3 hours at 900 g (Z10) for AuPd capsule. Droplets of gabbroic melt are present in the granitic matrix. Black crystals are quartz; bright crystals in gabbro, wuestite [also in (C)]. (**C**) Unsegregated composite droplet of gabbroic melt from a static experiment (1140°C, 0.7 GPa, and 12 hours). The
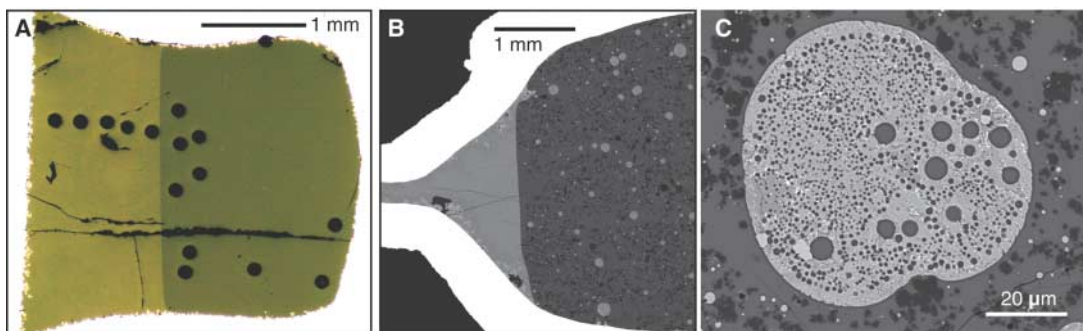
droplet has two generations of internal granitic droplets. Most of the droplet is composed by fayalite quench crystals; to the left, it has a single small homogeneous area of gabbroic melt.

lattice site model (8, 28), in which major cations are replaced by trace cations in a tetrahedral network-forming site or in a cation site coordinated by NBOs. This model precludes mixing between the two lattices and thus fails to explain the dependence of partition coefficients on the composition of melt pairs (28). Therefore, to rationalize and extrapolate the observed trace element partitioning, we formulate a model (18) for the melts as a mixture of a major network-modifying component, MO_n, a trace network-modifying component, BO_m, and a major polymerized component, C_oO_p. Melt excess energy is included at lowest order approximation (regular binary interactions). For our experimental system, MO_n is identified with FeO, whereas C_oO_p is taken to be a combination of $KAlO_2$ and SiO_2 so as to satisfy mass balance constraints. Optimization of the stoichiometric factor p to match the solvus symmetry required by the regular solution model yields a value of 5.96 ± 0.05, approximated here as $p = 6$. Assuming excess energy arises only through the interaction of the network-modifying components with the polymerized component, the molar trace element partition coefficient is

$$Q_{BO_m}^{gabbro/granite} = \exp\left[\left(1 - 2x_{MO_n}^{granite}\right)W_{BO_m-C_oO_p}'\right]$$

(1)

where $x_{MO_n}^{granite}$ is the mole fraction of MO_n in the granitic melt and $W_{BO_m-C_oO_p}' = W_{BO_m-C_oO_p}/RT$ is the dimensionless interaction parameter for BO_m-C_oO_p melt (18). The parameter $W_{BO_m-C_oO_p}'$ can be expressed in a more physically meaningful way as $W_{BO_m-C_oO_p}' = 2/T_{BO_m-C_oO_p}'$, where $T_{BO_m-C_oO_p}'$ is the homologous temperature measured relative to the critical temperature of the BO_m-C_oO_p solvus. Thus, Eq. 1 predicts trace element partitioning as a function of $T_{BO_m-C_oO_p}'$ and major element chemistry. The $x_{MO_n}^{granite}$-Q_{BO_m} trends calculated from the mean BO_m-C_oO_p critical temperatures inferred from Eq. 1 are consistent with the experimental trends (Fig. 3A), confirming the model dependence of trace element partition coefficients on the width of the miscibility gap. Additionally, the inferred BO_m-C_oO_p critical temperatures are comparable

to, but less than those of, the BO_m-SiO_2 solvii, a result consistent with the expectation that alumina in the C_oO_p component increases melt miscibility.

The effect of melt composition on trace element crystal-melt distribution predicted by the lattice strain model can be assessed by considering a generalized exchange reaction

$$BO_m + M \text{ crystal} = \frac{m}{n}MO_n + B \text{ crystal}$$

(2)
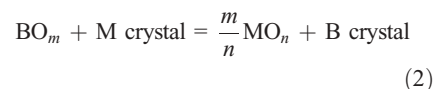
where M and B crystal represent the pure major and trace element limiting compositions of the crystalline phase, chosen so that a formula unit of pure B crystal contains 1 mol of B. In the context of our model (18), the trace element distribution coefficient is

$$Q_{BO_m}^{crystal/melt} = a_{M-crystal} \frac{\gamma_{BO_m}}{a_{MO_n}^{m/n}} \exp\left(-\frac{\Delta G_{strain}}{RT}\right)$$

(3)

where a_i and γ_i denote the thermodynamic activity and the activity coefficient, respectively, of species i and ΔG_{strain} is derived from the lattice strain model (5, 7). The second factor in Eq. 3 is the correction to the lattice strain model due to melt chemistry (Fig. 3C) and is expressed in terms of major element chemistry as

$$\frac{\gamma_{BO_m}}{a_{MO_n}^{m/n}} = \exp\left[(1 - x_{MO_n})\left\{W_{BO_m-C_oO_p}' - \right.\right.$$
$$\left.\left. W_{MO_m-C_oO_p}'\left[(1 - x_{MO_n})\frac{m}{n} + x_{MO_n}\right]\right\}\right]/x_{MO_n}^{m/n}$$

(4)

where $W_{MO_n-C_oO_p}'$ and $W_{BO_m-C_oO_p}'$ are known functions of the experimental observables $x_{MO_n}^{granite}$ and $Q_{BO_m}^{gabbro/granite}$. Taking x_{MO_n} as a proxy for the NBO/T ratio of silicate melts (Fig. 3) and noting that the nonlinearity arising from $m \neq n$ is weak for the oxides of interest, Eq. 4 implies, in the ideal limit and the limits $x_{MO_n} \to 0$ and $x_{MO_n} \to 1$, that the correction factor for melt composition is $x_{MO_n}^{-m/n}$ and that the correction factor will usually be less than the ideal value if $W_{MO_n-C_oO_p}' > W_{BO_m-C_oO_p}'$ (i.e., if BO_m partitions less strongly than MO_n into the more polymerized melt). Thus, although melt composition can cause a 10-fold increase in partition coefficients [e.g., Zr and Hf (Fig. 3C)], nonideality can also lead to situations in which the uncorrected lattice strain model is valid over most of the range of natural melt compositions [e.g., Zn (Fig. 3C)].

In our model, partition coefficients depend on the width of the MO_n-C_oO_p solvus and the BO_m-C_oO_p solvus critical temperature. Certain minor elements, notably P and Ti, increase the width of silicate liquid solvi (8, 29) but are not explicitly accounted for in the model. The model
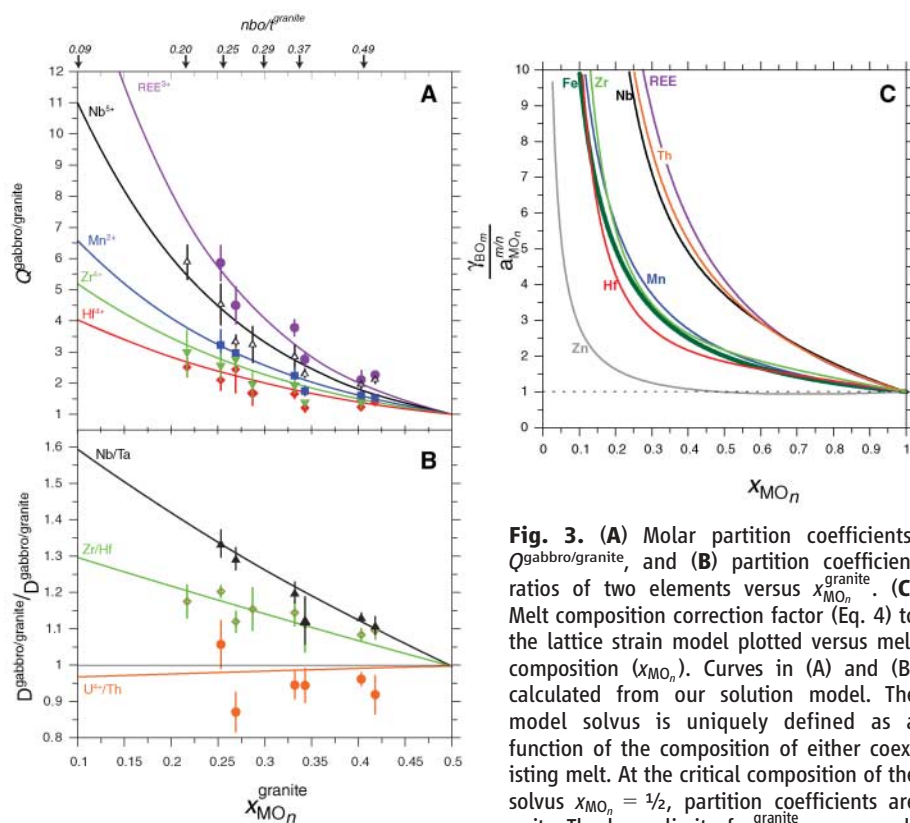

Fig. 3. (**A**) Molar partition coefficients, $Q^{gabbro/granite}$, and (**B**) partition coefficient ratios of two elements versus $x_{MO_n}^{granite}$. (**C**) Melt composition correction factor (Eq. 4) to the lattice strain model plotted versus melt composition (x_{MO_n}). Curves in (A) and (B) calculated from our solution model. The model solvus is uniquely defined as a function of the composition of either coexisting melt. At the critical composition of the solvus $x_{MO_n} = \frac{1}{2}$, partition coefficients are unity. The lower limit of $x_{MO_n}^{granite}$ corresponds to a degree of melt polymerization normally not exceeded by granites resulting from crystal fractionation processes. Thus, intercept values for partition coefficients on the vertical axis represent the maximum effect of melt composition during magma crystallization processes, reaching $Q_{REE}^{granite/gabbro} = 16.4$ for REE, which corresponds to $D_{REE}^{granite/gabbro} \approx 30$. Significant fractionation between the geochemical pairs Nb/Ta and Zr/Hf is obtained as a function of melt composition, but not for other pairs such as U^{4+}/Th. The values plotted along the upper axis are melt polymerization as expressed by the commonly used fraction of nonbridging oxygens over tetrahedra (NBO/T) in the granite, calculated after (27). Natural melt compositions (x_{MO_n}) in fractionation and partial melting processes are in the range from 0.1 to 0.7.

reproduces the observed distribution coefficients in both P-rich and P-poor experiments. This behavior implies that phosphorous, at least at geologically relevant concentration levels, does not influence partition coefficients through complexing with trace cations, as proposed by (28), but rather influences partitioning indirectly by affecting NBO/BO ratios. Specifically, elements such as P with high coordination numbers lower the melt NBO/BO ratio and decrease the configurational entropy of the melt, an effect that widens the MO_n-C_oO_p solvus and increases melt-melt partition coefficients. Within the di- and trivalent cations, such a tendency is observable in our data; i.e., partition coefficients decrease with decreasing coordination number.

Our data imply that a significant change in the shape of the lattice-strain model parabola will result for the alkalis. To quantify this effect, we used data sets of $D^{cpx/basalt}$ (30, 31) for basalts analogous to the gabbroic melt of experiment Z10 and combine $D^{cpx/basalt}$ with our $D^{basalt/granite}$. The site parameters for monovalent cations calculated from $D^{cpx/granite}$ with respect to $D^{cpx/basalt}$ are characterized by a Young's modulus decreased by 16 to 35% and by a strain-free partition coefficient D_0 increased by a factor of 2. This softening of the site is attributed to the effect of melt composition. For the cations coordinated to NBOs, the effect of melt composition will increase $D^{crystal/melt}$, D_o, and hence the position of the parabola with respect to the D coordinate (1, 5) by one order of magnitude when changing from basaltic to granitic melt compositions. This effect acts in concert with the changes in crystal composition that occur as a consequence of the change in melt composition. Melt composition will play a key role for elements whose crystal/melt partition coefficients are close to unity, because they may change from compatible to incompatible as a function of melt composition. Because of the relative uniformity of partition coefficients for traces of Ca, Mg, RE, transition, and high field strength elements, melt composition does not strongly affect the relative partition coefficients of these elements. The latter are in general well characterized by models describing relative crystal-melt partition coefficients solely in terms of crystal lattice strain, but to quantify individual partition coefficients an explicit melt compositional term such as in Eq. 4 is necessary. Gross exceptions to the above generality are Pb (Fig. 2), for which $D^{gabbro/granite}$ is as much as two orders of magnitude different from other divalent cations, and to a lesser extent Ba, Zn, and Sn. Among the NBO-coordinated cations, variations of $D^{basalt/granite}$ up to a factor of 2 exist, a nonnegligible effect in the context of geochemical melting models.

References and Notes

1. N. Onuma, H. Higuchi, H. Wakita, H. Nagasawa, *Earth Planet. Sci. Lett.* **5**, 47 (1968).
2. J. C. Brice, *J. Cryst. Growth* **28**, 249 (1975).
3. S. Banno, Y. Matsui, *Chem. Geol.* **11**, 1 (1973).
4. M. J. Drake, D. F. Weill, *Geochim. Cosmochim. Acta* **39**, 689 (1975).
5. J. D. Blundy, B. J. Wood, *Nature* **372**, 452 (1994).
6. B. J. Wood, J. D. Blundy, *Geochim. Cosmochim. Acta* **66**, 3647 (2002).
7. B. J. Wood, J. D. Blundy, *Contrib. Mineral. Petrol.* **129**, 166 (1997).
8. E. B. Watson, *Contrib. Mineral. Petrol.* **56**, 119 (1976).
9. F. J. Ryerson, P. C. Hess, *Geochim. Cosmochim. Acta* **42**, 921 (1978).
10. B. O. Mysen, D. Virgo, *Geochim. Cosmochim. Acta* **44**, 1917 (1980).
11. R. L. Linnen, H. Keppler, *Geochim. Cosmochim. Acta* **66**, 3293 (2002).
12. B. O. Mysen, E. V. Dubinsky, *Geochim. Cosmochim. Acta* **68**, 1617 (2004).
13. M. W. Schmidt, A. Dardon, G. Chazot, R. Vannucci, *Earth Planet. Sci. Lett.* **226**, 415 (2004).
14. S. Klemme, S. Prowatke, K. Hametner, D. Günther, *Geochim. Cosmochim. Acta* **69**, 2361 (2005).
15. I. V. Veksler, C. Petibon, G. A. Jenner, A. M. Dorfman, D. B. Dingwell, *J. Petrol.* **39**, 2095 (1998).
16. E. Roedder, *Geochim. Cosmochim. Acta* **42**, 1597 (1978).
17. W. Visser, A. F. K. VanGroos, *Am. J. Sci.* **279**, 70 (1979).
18. Material and methods are available as supporting material on *Science* Online.
19. Previous studies (8, 9) have shown that 14 hours are sufficient to reach chemical equilibrium in this temperature range; we thus generally doubled this run time.
20. R. L. Lange, I. S. E. Carmicheal, *Rev. Mineral.* **24**, 25 (1990).
21. At 1180°C, the two melts have SiO_2 contents of 72.2 and 37.1 weight %; at 1210°C, the immiscibility gap is closed, which is in excellent agreement with (16, 17).
22. Electronegativities are from (32).
23. R. D. Shannon, *Acta Cryst.* **A32**, 751 (1976).
24. Ionic radii are those for the dominant coordination number as listed in table S1.
25. L. Galoisy et al., *Mineral. Mag.* **64**, 409 (2000).
26. F. J. Ryerson, P. C. Hess, *Geochim. Cosmochim. Acta* **44**, 611 (1980).
27. B. O. Mysen, *Structures and Properties of Silicate Melts,* vol. 4 of *Developments in Geochemistry* (Elsevier, Amsterdam, 1988).
28. A. J. G. Ellison, P. C. Hess, *Geochim. Cosmochim. Acta* **53**, 1965 (1989).
29. W. Visser, A. F. K. VanGroos, *Am. J. Sci.* **279**, 970 (1979).
30. J. D. Blundy, J. Dalton, *Contrib. Mineral. Petrol.* **139**, 356 (2000).
31. R. A. Brooker et al., *Nature* **423**, 738 (2003).
32. R. D. Lide, Ed., *The Handbook of Chemistry and Physics* (CRC Press, Boca Raton, FL, ed. 85, 2005), table 9-74.
33. W. R. H. Ramsey, A. J. Crawford, J. D. Fodon, *Contrib. Mineral. Petrol.* **88**, 386 (1984).
34. H. Sorenson, Ed., *The Alkaline Rocks* (Wiley, Letchworth, UK, 1974), p. 117.
35. We thank N. Baker from *g-max* for building the centrifuge and K. Hametner for help with the LA-ICP-MS analyses. M.W.S. acknowledges Swiss National Science Foundation grant no. 2-77182-02 for financing part of the centrifuge.

p53 Regulates Mitochondrial Respiration

Satoaki Matoba,[1] Ju-Gyeong Kang,[1] Willmar D. Patino,[1] Andrew Wragg,[1] Manfred Boehm,[1] Oksana Gavrilova,[2] Paula J. Hurley,[3] Fred Bunz,[3] Paul M. Hwang[1]*

The energy that sustains cancer cells is derived preferentially from glycolysis. This metabolic change, the Warburg effect, was one of the first alterations in cancer cells recognized as conferring a survival advantage. Here, we show that p53, one of the most frequently mutated genes in cancers, modulates the balance between the utilization of respiratory and glycolytic pathways. We identify Synthesis of Cytochrome c Oxidase 2 (SCO2) as the downstream mediator of this effect in mice and human cancer cell lines. SCO2 is critical for regulating the cytochrome c oxidase (COX) complex, the major site of oxygen utilization in the eukaryotic cell. Disruption of the *SCO2* gene in human cancer cells with wild-type p53 recapitulated the metabolic switch toward glycolysis that is exhibited by p53-deficient cells. That SCO2 couples p53 to mitochondrial respiration provides a possible explanation for the Warburg effect and offers new clues as to how p53 might affect aging and metabolism.

Cancer is a genetic disease caused by the dysregulation of various cellular pathways that orchestrate cell growth and death (1). It is clear that some of these pathways must modulate cellular metabolism. As described by Otto Warburg in 1931, cancer cells preferentially utilize glycolytic pathways for energy generation while down-regulating their aerobic respiratory activity (2). A number of mechanisms have been proposed to explain the Warburg effect (3–7), but there have not been any reports of a genetically defined path-

way that couples a tumor suppressor gene to mitochondrial aerobic respiration.

Critical to aerobic life is the cytochrome c oxidase (COX) complex in the mitochondrion, where most of the molecular oxygen is consumed in the eukaryotic cell. In cancer cells mitochondrial respiratory activity is decreased in association with changes in the expression levels of COX complex subunit proteins, but the genetic mechanisms that underlie their modulation are unclear (8, 9). We reasoned that because the metabolic alterations of cancer cells are